mater.scichina.com link.springer.com

Published online 28 July 2022 | https://doi.org/10.1007/s40843-022-2113-y
Sci China Mater 2023, 66(1): 241–248

Controllable volatile-to-nonvolatile memristive switching in single-crystal lead-free double perovskite with ultralow switching electric field

Qi You[1], Fu Huang[1], Feier Fang[2], Jiaqi Zhu[1], Yue Zheng[1], Shaofan Fang[2], Bo Zhou[2], Henan Li[2], Cheng Han[1*] and Yumeng Shi[2*]

ABSTRACT All-inorganic lead-free double perovskite offers a potential material platform for electronic or optoelectronic memory devices owing to its ionic migration-based electrical transport, high photosensitivity, low toxicity, and environmental stability. However, the commonly used polycrystalline perovskite films severely restrict device performance. Herein, we demonstrate a high-performance memristor based on single-crystal double perovskite $Cs_2AgBiBr_6$ with an ultralow switching electric field of 6.67×10^4 V m^{-1} and a high current on/off ratio of 10^7. Remarkably, the resistive switching of $Cs_2AgBiBr_6$ is found to be thickness-dependent, which evolves from volatile threshold to nonvolatile resistance switching with the crystal thickness from 100 to 800 nm. Elemental analysis reveals that the formation of conductive channels in $Cs_2AgBiBr_6$ is associated with the migration of Br vacancies with low activation energy. In addition, the formed conductive channels can be annihilated by light illumination with controlled wavelength and intensity, which leads to the realization of optoelectronic memories with separate electrical-writing and optical-erasing processes. Our findings provide deep insights into the ionic migration in single-crystal perovskite and pave the way for its future application in electronic and optoelectronic memory devices.

Keywords: single-crystal double perovskite, $Cs_2AgBiBr_6$, volatile-to-nonvolatile switching, memristor, switching electric field

INTRODUCTION

The memristor, an elemental electronic device with resistive switching characteristics, has been identified as a promising candidate for the next-generation nonvolatile random access memory, which can serve as the building blocks in artificial neuromorphic systems to overcome the von Neumann bottleneck in conventional computing architectures. Memristors are generally organized into highly interconnected crossbar arrays in artificial neural networks, which are free of data transmission between memory and processing units and thus maximize the computation speed and energy efficiency [1]. Traditional memristors are generally built on binary metal oxides, such as TaO_x, HfO_x, and TiO_x [2–4]. However, these oxides usually have a high operation voltage due to the high activation energy of oxygen vacancies, and they also involve a high-temperature growth process that is not suitable for flexible electronics [5].

The emergence of organic-inorganic lead halide perovskite (OLHP), represented by $CH_3NH_3PbI_3$, has initiated the exploration of a new material system for a wide range of electronic and optoelectronic applications including memories [6,7], solar cells [8–10], photodetectors [11–13], light-emitting diodes [14], and lasers [15], owing to their high photosensitivity, simple solution-based preparation, and abundant material choice. Notably, the use of perovskite as the active layer in memristors has attracted great attention by taking advantage of its high defect tolerance and intrinsic ionic migration [16–18]. However, the toxicity of lead and the low air stability of OLHP pose substantial challenges to its commercialization process, particularly in terms of environmental issues. Furthermore, the polycrystalline perovskite films with rich defects and grain boundaries are generally employed to construct memristors, which severely affects the device performance, e.g., reducing the carrier mobility or generating high leakage current. Thus, the development of single-crystal perovskite with high environmental stability and memristive performance is highly desirable.

All-inorganic lead-free double perovskite with the structure of $A_2B^IB^{III}X_6$ (A = Cs, Rb; B^I = Ag, K, Na, Li; B^{III} = Bi, Sb, In; X = I, Br, Cl) is a promising choice for realizing stable and environment-friendly devices, which can be formed through the substitution of two toxic Pb^{2+} in the crystal lattice with a pair of non-toxic heterovalent (i.e., monovalent and trivalent) metal cations [19,20]. Among them, $Cs_2AgBiBr_6$ stands out due to its unique features, which include a long carrier lifetime, a small carrier effective mass, and low toxicity [21]. Furthermore, due to its high photo-absorption efficiency and excellent stability under ambient conditions, $Cs_2AgBiBr_6$ has been extensively investigated for various optoelectronic applications, including photodetection, photovoltaics, and photocatalysis [22–25]. Polycrystalline $Cs_2AgBiBr_6$ thin films have been reported as the channel material in memristors [26,27]. Cheng *et al.* [26] proposed a sandwiched structure of indium tin oxide (ITO)/$Cs_2AgBiBr_6$/Au for memristors, which exhibits excellent tolerance to harsh environments such as high moisture, temperature, and radiation. However, the device requires a relatively high switching electric field of 5×10^6 V m^{-1} and also presents a low current on/off ratio of 100. The Ag/polymethylmethacrylate (PMMA)/$Cs_2AgBiBr_6$/ITO memristor has been utilized to successfully emulate the synaptic plasticity in biological neural

[1] International Collaborative Laboratory of 2D Materials for Optoelectronics Science and Technology of Ministry of Education, Institute of Microscale Optoelectronics, Shenzhen University, Shenzhen 518060, China
[2] College of Electronics and Information Engineering, Shenzhen University, Shenzhen 518060, China
[*] Corresponding authors (emails: hancheng@szu.edu.cn (Han C); yumeng.shi@szu.edu.cn (Shi Y))

 © Science China Press and Springer-Verlag GmbH Germany, part of Springer Nature 2022

systems, and yet the device performance is limited by the weak resistive switching (on/off ratio < 10) [27]. Constructing devices on single-domain macroscopic crystals would dramatically boost the memristive performance due to the significantly reduced defects and grain boundaries. Very recently, Mao *et al.* [28] reported a monocrystalline $Cs_3Sb_2Br_9$ perovskite-based memristor with a record-low switching electric field of 2.2×10^5 V m^{-1} and a high on/off ratio of 10^6, as well as research on the influence of channel length on the device performance. However, memristors based on single-crystal double perovskite have not yet been reported, and the impact of perovskite thickness on its resistive switching performance still remains unclear. Moreover, one of the fascinating properties of perovskite is its strong light absorption. The fact how the incident light affects memristive behaviors of single-crystal perovskite has been rarely explored.

In this study, a single-crystal $Cs_2AgBiBr_6$-based memristor with thickness-dependent resistive switching is presented. The device exhibits an ultralow switching electric field of 6.67×10^4 V m^{-1} and a high current on/off ratio up to 10^7. Its switching behavior transits from volatile threshold to nonvolatile resistance switching when the thickness of $Cs_2AgBiBr_6$ is increased from 100 to 800 nm. Energy-dispersive X-ray (EDX) spectroscopy analysis reveals that the conductive channel of $Cs_2AgBiBr_6$ is formed by the motion of Br vacancies with low activation energy. In addition, light illumination with controlled intensity and wavelength can be used to annihilate the formed conductive channel, which results in an optoelectronic memory with a separate electrical-writing and optical-erasing process.

EXPERIMENTAL SECTION

Synthesis of single-crystal $Cs_2AgBiBr_6$ nanoflakes

The sapphire (0001) substrates were sequentially rinsed in acetone, isopropanol, and deionized water for 5 min by sonication and then were dried by the blowing of nitrogen. An oxygen plasma treatment (50 W for 5 min) was used to further clean the substrates. The powders of CsBr (42.6 mg), $BiBr_3$ (44.9 mg), and AgBr (18.8 mg) were completely dissolved in 5 mL HBr (47%) by heating the solution at 120°C for 2 h to obtain the precursor solution. A drop of $Cs_2AgBiBr_6$/hydrobromic acid precursor (20 μL, 0.02 mol) was dropped over the plasma-treated sapphire substrate, which was subsequently covered with a bare Si wafer. The sample was heated for 48 h on a hotplate at 80°C, with a weight placed on the Si wafer. To regulate the thickness of the as-grown $Cs_2AgBiBr_6$, the pressure on the substrate was controlled to 40/30/20/10 kPa by altering the weight. The upper wafer was then removed, which left the $Cs_2AgBiBr_6$ nanoflakes on the sapphire substrates.

Fabrication of $Cs_2AgBiBr_6$-based memristor

A copper mesh with a gap of 15 μm was used as a shadow mask to precisely cover the target $Cs_2AgBiBr_6$ nanoflakes under an optical microscope, followed by the fixing of the mask using scotch tape. After the thermal evaporation of Au at a rate of 0.2 Å s^{-1}, symmetric electrodes with a thickness of 100 nm were formed on the $Cs_2AgBiBr_6$, and the sample was cooled down to room temperature.

Characterizations and device measurements

The atomic force microscopy (AFM) characterizations were carried out using a BRUKERMultiMode 8 microscope (Tip Model: SCANASYST-AIR, Material: Silicon Tip on Nitride Lever). The NanoScope software was used for data analysis and image processing. The high-angle annular dark-field scanning transmission electron microscopy (HAADF-STEM) images were obtained by using a Titan Cubed Themis G2 300 microscope operating at 300 kV equipped with a spherical aberration corrector. An X-ray diffractometer (Rigaku, Ultima IV, Sevenoaks, UK) with the excitation source of Cu Kα (λ = 1.5418 Å) was used to measure the X-ray diffraction (XRD) patterns. Raman and photoluminescence (PL) spectra were obtained on a microscopic confocal Raman system (Witec Alpha 300) with a laser at 532 and 450 nm, respectively. Ultraviolet-visible (UV-Vis) absorption spectroscopy was carried out using a UV-Vis-near-infrared (NIR) spectrophotometer (UV-3600PLUS, Shimadzu). The electrical transport properties of devices were characterized by a ScanPro Advance probe station configured with a Keithley 2636B Source-Measure Unit. Field-emission scanning electron microscopy (SEM) and EDX spectroscopy characterizations were implemented on a Thermo APREO S SEM system. All the measurements were undertaken at room temperature.

RESULTS AND DISCUSSION

Single-crystal $Cs_2AgBiBr_6$ nanoflakes were produced on the sapphire (0001) substrate by a simple space-confined method according to a previous report [29]. The AFM image in Fig. 1a shows that the thickness of a typical as-grown nanoflake is ~800 nm, and the inset optical microscopy image clearly shows homogeneous triangular islands with a length of 60–80 μm. In order to clarify the pure phase of $Cs_2AgBiBr_6$, the XRD pattern was measured (Fig. 1b), which presents three dominant diffraction peaks of (111), (222), and (333) planes, in good agreement with the standard simulation results. This indicates the (111)-oriented crystallinity of the as-prepared nanoflake, and the hexagonal feature of the (111) plane leads to the preferential growth of triangular $Cs_2AgBiBr_6$ crystals [30]. The cross-sectional HAADF-STEM characterization of $Cs_2AgBiBr_6$ further confirms its single-crystallinity (Fig. S1). The Raman spectrum of $Cs_2AgBiBr_6$ exhibits three characteristic peaks nearly located at 74, 139, and 179 cm^{-1} (Fig. 1c), corresponding to different vibration modes, labeled as T_{2g}, E_{1g}, and A_{1g}, respectively [29,31]. The optical properties of $Cs_2AgBiBr_6$ were further studied by UV-Vis absorption and PL characterizations, as shown in Fig. 1d. The absorbance onset is aligned at nearly 540 nm and a sharp absorption peak appears at a wavelength of 440 nm [29].

Fig. 2a shows the optical microscopy image and schematic device structure of the memristor with the crystal structure of the active layer $Cs_2AgBiBr_6$ shown in the left upper corner. Thermal evaporation was used to deposit Au electrodes with a thickness of 100 nm on the $Cs_2AgBiBr_6$ nanoflake to form a planar Au/$Cs_2AgBiBr_6$/Au device structure with a channel length of about 15 μm between the Au electrodes. Through voltage loop sweeping, two types of resistive switching, threshold and resistance switching, were identified in the $Cs_2AgBiBr_6$-based memristors, as illustrated in Fig. 2b, c, respectively. For threshold switching, the high-resistance state (HRS) of the device suddenly transited to a low-resistance state (LRS) at 1.02 V (termed a SET process), which spontaneously relaxed to the initial HRS at a close-to-zero bias (termed as a RESET process), corresponding to typical volatile switching behavior. The subsequent negative sweeping induced a symmetric current-voltage (I-V) character-

 © Science China Press and Springer-Verlag GmbH Germany, part of Springer Nature 2022

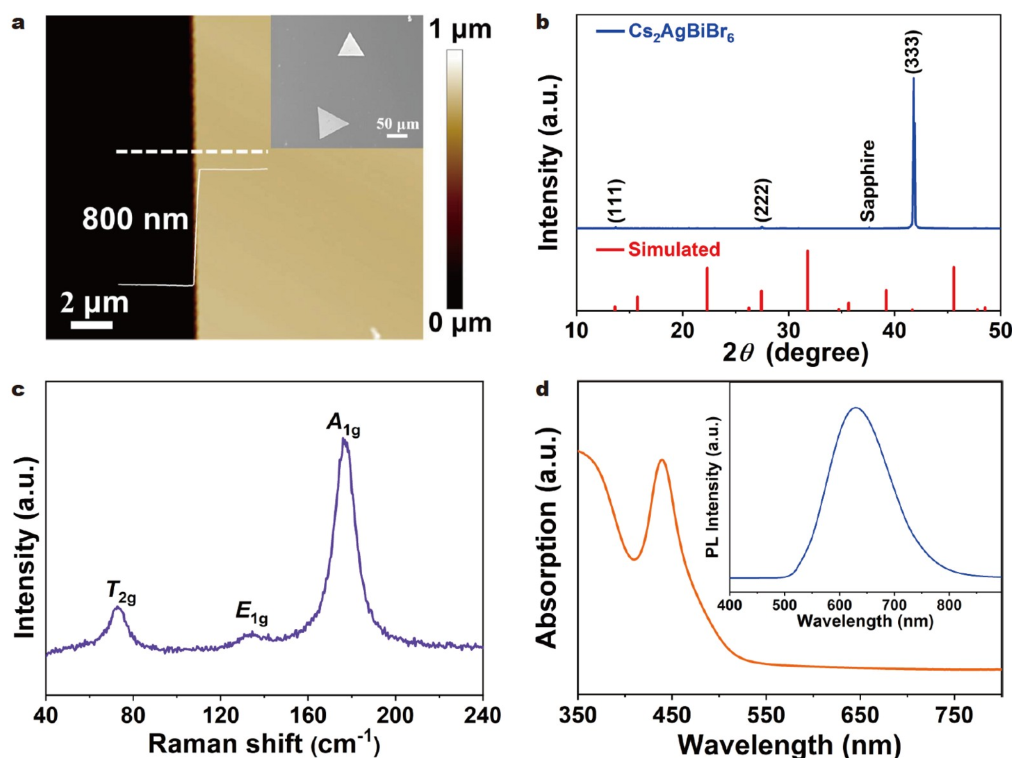

Figure 1 (a) AFM image of an as-synthesized $Cs_2AgBiBr_6$ nanoflake with the height profile along the white dotted line (inset: the optical microscopy image of $Cs_2AgBiBr_6$ nanoflakes on the sapphire (0001) substrate). (b) XRD spectrum of $Cs_2AgBiBr_6$. The standard XRD pattern was simulated using the "diamond" software. (c) Raman and (d) UV-Vis absorption (inset: PL) spectra of the single-crystal $Cs_2AgBiBr_6$ on the sapphire substrate.

istic with the SET voltage (V_{set}) located at −0.92 V [32,33]. For resistance switching, the device was switched on at 1.02 V V_{set} for resistance switching and did not revert to the original HRS until a negative voltage of −8.59 V was applied, which indicates nonvolatile switching [26,28,34]. Both switching behaviors exhibit a high current on/off ratio of 10^7 due to the exceptionally low off current of 10^{-12} A. Statistical analysis over 25 devices indicates a Gaussian distribution of the V_{set} with an average value of 1 V, as shown in Fig. 2d, presenting excellent repeatability of $Cs_2AgBiBr_6$ memristors with low V_{set}. The retention time of our device was also measured at room temperature to evaluate its nonvolatile capability (Fig. S2), where the LRS can be maintained for more than 700 s without significant degradation at a read voltage of 0.2 V.

We further explored the memristive performance of $Cs_2AgBiBr_6$ under different compliance currents (I_{cc}). The V_{set} was nearly maintained at 1 V when increasing the I_{cc} from 10^{-10} to 10^{-5} A, suggesting high device stability. In particular, all the devices present pure threshold switching for the I_{cc} set below 10^{-6} A. Similar phenomena have been reported by Zhang *et al.* [35], which can be understood by the formation of fragile conductive filaments (CFs) in the channel caused by a low I_{cc}, thus leading to volatile switching. At the I_{cc} of 10^{-6} A, the device also maintains good switching behavior for over 80 cycles under continuous electrical measurement (Fig. S3). Moreover, the memristor can be operated with an I_{cc} as low as 10^{-10} A, showing the potential of $Cs_2AgBiBr_6$ in low-power applications. Overall, both threshold and resistance switching can be achieved in $Cs_2AgBiBr_6$ with an on/off ratio of up to 10^7 and an average V_{set} of 1 V. The average switching electric field (E_{set}) was determined to be 6.67×10^4 V m^{-1} based on the channel length of 15 μm, which is among the lowest values in previously reported memristors. The comparison of the on/off ratio and the $1/E_{set}$ of our device with the literature is displayed in Fig. 2f [6,28,35–48], which demonstrates the outstanding memristive performance of the single-crystal $Cs_2AgBiBr_6$.

In order to regulate the switching type and understand the switching mechanism, $Cs_2AgBiBr_6$ nanoflakes with thicknesses varying from 70 to 800 nm were used to fabricate memristors (their morphologies are shown in Figs S4 and S5). After the periodic sweeping of voltage, the 300-, 600-, and 800-nm-thick nanoflakes display both threshold and resistance switching with varying probabilities (Fig. 3a, b), while the 100 nm-thick $Cs_2AgBiBr_6$ presents only threshold switching (Fig. S5a, b). It should be noted that no obvious resistive variation was observed for the 70-nm device by increasing the voltage to 20 V, indicating a failure to form CFs in such a thin flake (Fig. S5c, d). In Fig. 3c, the statistically-extracted V_{set} is shown against the thickness of $Cs_2AgBiBr_6$, where the average V_{set} gradually decreased from 10.6 to 1 V when the thickness grew from 100 to 800 nm. This reduced V_{set} indicates the easier formation of CFs under the external voltage in the thicker $Cs_2AgBiBr_6$ nanoflakes. The probability for the appearance of threshold and resistance switching in an individual memristor as a function of $Cs_2AgBiBr_6$ thickness is summarized in Fig. 3d, among which the resistance probability was significantly increased from 0% to 80% as the thickness increased from 100 to 800 nm, thus implying a transition from threshold to resistance switching (Fig. S6).

The formation and rupture of CFs enabled by ionic migration are primarily responsible for the resistive switching in perovskite-based memristors. The two mainstream memristive

 © Science China Press and Springer-Verlag GmbH Germany, part of Springer Nature 2022

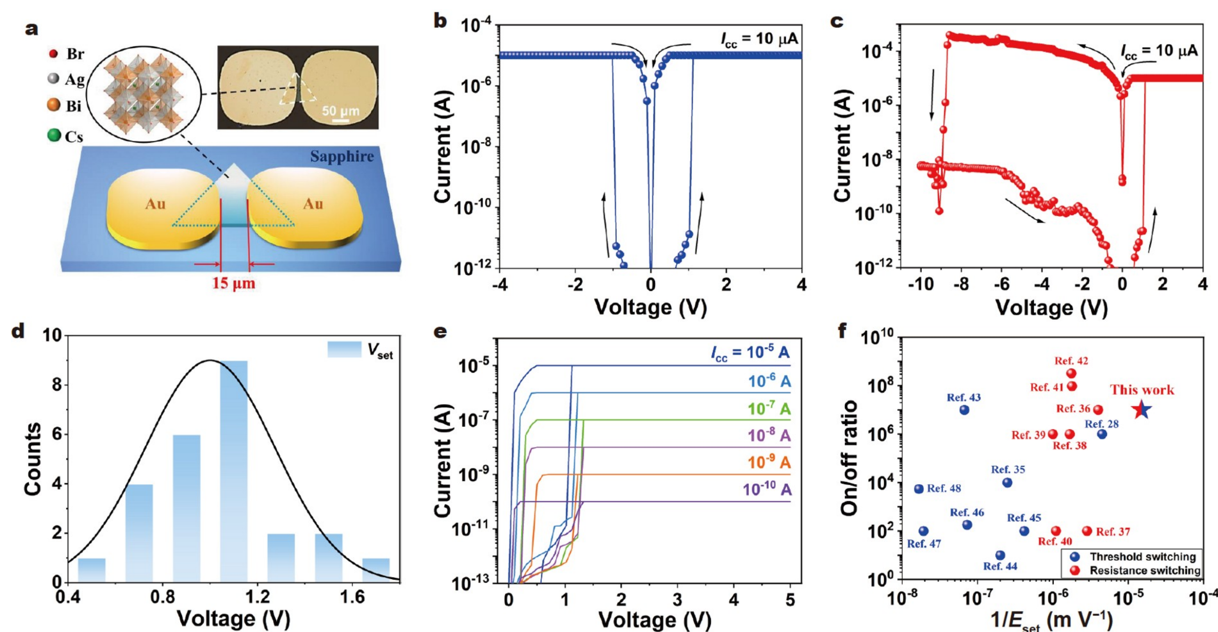

Figure 2 (a) Schematic diagram and optical microscopy image of the as-fabricated $Cs_2AgBiBr_6$ memristors. The crystal structure of $Cs_2AgBiBr_6$ is illustrated in the left upper corner. The typical *I-V* characteristics of (b) threshold and (c) resistance switching are obtained in $Cs_2AgBiBr_6$ memristors. (d) Histogram of SET voltage extracted over 25 devices. This can be fitted by a Gaussian distribution with an average of 1 V. (e) Threshold switching behaviors of $Cs_2AgBiBr_6$ under different compliance currents. (f) The comparison of the current on/off ratio and $1/E_{set}$ of $Cs_2AgBiBr_6$ memristors with the literature.

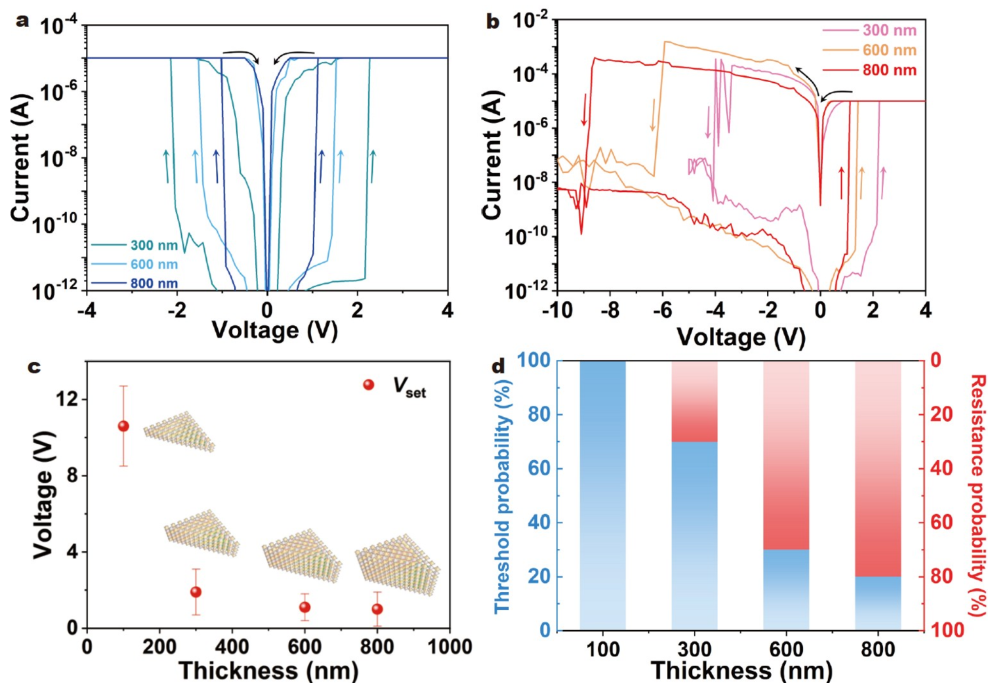

Figure 3 *I-V* characteristics of 300-, 600-, 800-nm-thick $Cs_2AgBiBr_6$ with both (a) threshold and (b) resistance switching. (c) The statistically extracted SET voltage as a function of $Cs_2AgBiBr_6$ thickness. (d) Probability for the emergence of threshold and resistance switching in an individual device with respect to the $Cs_2AgBiBr_6$ thickness.

switching mechanisms are electrochemical metallization memory (ECM) and valence change memory (VCM), which depend on the migration of metallic and vacancy ions, respectively [49]. The switching behavior of our Au/$Cs_2AgBiBr_6$/Au devices is ascribed to the formation/rupture of vacancy-formed CFs due to the inert Au electrodes [16,28]. In the double perovskite $Cs_2AgBiBr_6$, there are potentially four types of vacancies, labeled as V_{Cs}, V_{Ag}, V_{Bi}, and V_{Br}, where the CFs tend to be formed by the migration of ions with low activation energy. The activation energy for Cs, Bi, Ag, and Br vacancies in $Cs_2AgBiBr_6$ has been estimated to be 1.413, 3.363, 0.895, and 0.438/0.427 eV (Br1/Br2) in previous work [50], suggesting the most likely migration of Br

 © Science China Press and Springer-Verlag GmbH Germany, part of Springer Nature 2022

vacancies to produce CFs. Furthermore, the corner-sharing octahedral structure of $Cs_2AgBiBr_6$ allows the hopping of V_{Br} within the half of the unit cell and facilitates its migration between adjacent bromide sites along the equatorial plane under an external electric field, whereas the migration of Cs, Ag, and Bi along the pathway across one cell would severely deteriorate the crystal structure [7]. As a result, the highly mobile V_{Br} with low activation energy may be responsible for the high-performance memristive switching in the single-crystal $Cs_2AgBiBr_6$. Fig. 4a depicts a hypothetical scenario for the formation/rupture of V_{Br} CFs in $Cs_2AgBiBr_6$ with different thicknesses. For thin $Cs_2AgBiBr_6$, the fragile CFs are formed under external bias, which is sensitive to the thermally driven diffusion of V_{Br} and results in the spontaneous RESET of the HRS at a close-to-zero bias. As the thickness of $Cs_2AgBiBr_6$ increases, more Br vacancies are involved in the formation of CFs, thus leading to a stable conductive channel that needs to be RESET by a large reverse bias [28].

To figure out the ionic species involved in the memristive switching process, EDX spectroscopy measurements were performed to analyze the elemental distribution of $Cs_2AgBiBr_6$ nanoflakes with different thicknesses before and after CF formation. Fig. 4b shows an SEM image of a $Cs_2AgBiBr_6$ channel between two Au electrodes, with EDX scanning implemented across the channel (i.e., along the orange dotted line). The intensity distributions of Br (Lα1, Lα2) and Ag (Lα) signals in 100- and 300-nm-thick $Cs_2AgBiBr_6$ are displayed in Fig. 4c–f (the corresponding EDX spectra for each element are shown in Fig. S7). The Br intensity decreased significantly after formation, while the signals of Ag (Lα), Bi (Mα), and Cs (Lα) were almost unchanged (Fig. S8a, b, e and f), which reveals the migration of Br ions toward the anode and its dominant role in determining the switching behavior of $Cs_2AgBiBr_6$. Similar phenomena were also found in the $Cs_2AgBiBr_6$ with the thickness of 600 and 800 nm (Figs S9a–d and S8c, d, g, h). In Fig. 4g, the atomic ratio of the pristine state to forming state for Br and Ag was statistically extracted in the channel region and displayed with regard to the $Cs_2AgBiBr_6$ thickness. The average atomic ratio of Br was found to be remarkably increased from ~1.54 to ~2.56, with the thickness growing from 100 to 800 nm, which indicates the migration of more Br vacancies in the thicker $Cs_2AgBiBr_6$, hence resulting in the formation of more stable CFs and higher probability of nonvolatile switching. Furthermore, the linear fitting of the *I-V* curve under the SET process in Fig. 2c under the SET process implies transport in $Cs_2AgBiBr_6$ follows the space-charge limited conduction (SCLC) model, which further supports the conductive filamentary behavior based on V_{Br} [26] (Fig. S10).

Last but not least, the impact of light illumination on ionic migration in the single-crystal $Cs_2AgBiBr_6$ (800 nm thick) was carefully examined. The channels of memristors were irradiated with broadband light from 300 to 800 nm with tunable intensity. During the SET process, the V_{set} steadily increased from 1.4 to 3.8 V upon the white light, with the intensity increased from 0 to 4.09 mW cm^{-2} (Fig. 5a), suggesting the suppression of CF formation by incident light. Under illumination with variable wavelengths from 365 to 660 nm at a fixed intensity, the device exhibits a similar increase in V_{set} that peaks at 455 nm, as shown in Fig. 5b. This wavelength-dependent V_{set} agrees well with the absorption spectrum of $Cs_2AgBiBr_6$ (Fig. 1d), further demonstrating the light-induced attenuation of CFs. The statistically calculated V_{set} is also plotted as a function of light intensity and wavelength in Fig. 5c. Furthermore, the CFs in $Cs_2AgBiBr_6$ can be annihilated by prolonging the irradiation time, as clearly observed in the time-dependent response (Fig. 5d). By applying a constant voltage of 5 V in the dark, the device was initially SET

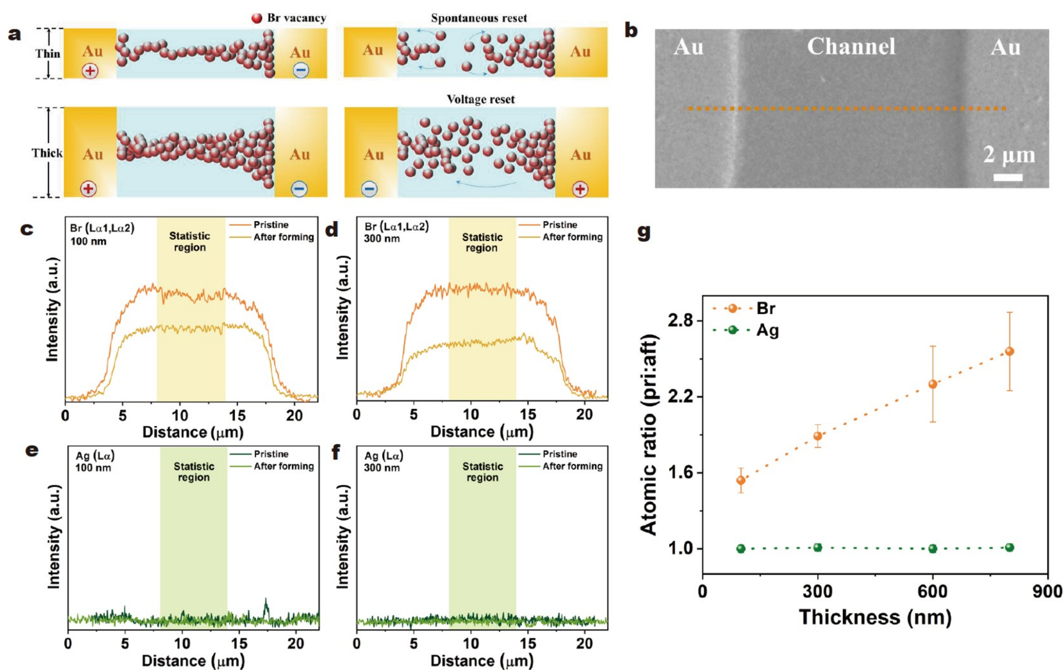

Figure 4 (a) Schematic illustration of the SET and RESET mechanism in $Cs_2AgBiBr_6$ with different thicknesses. (b) SEM image of the channel region of the $Cs_2AgBiBr_6$ memristor. EDX scanning was performed along the orange dotted line. EDX signal distribution for (c, d) Br and (e, f) Ag in the $Cs_2AgBiBr_6$ channel with the thickness of 100 and 300 nm, respectively. (g) The atomic ratio of the pristine state to forming state for Br and Ag in the channel with respect to the $Cs_2AgBiBr_6$ thickness.

 © Science China Press and Springer-Verlag GmbH Germany, part of Springer Nature 2022

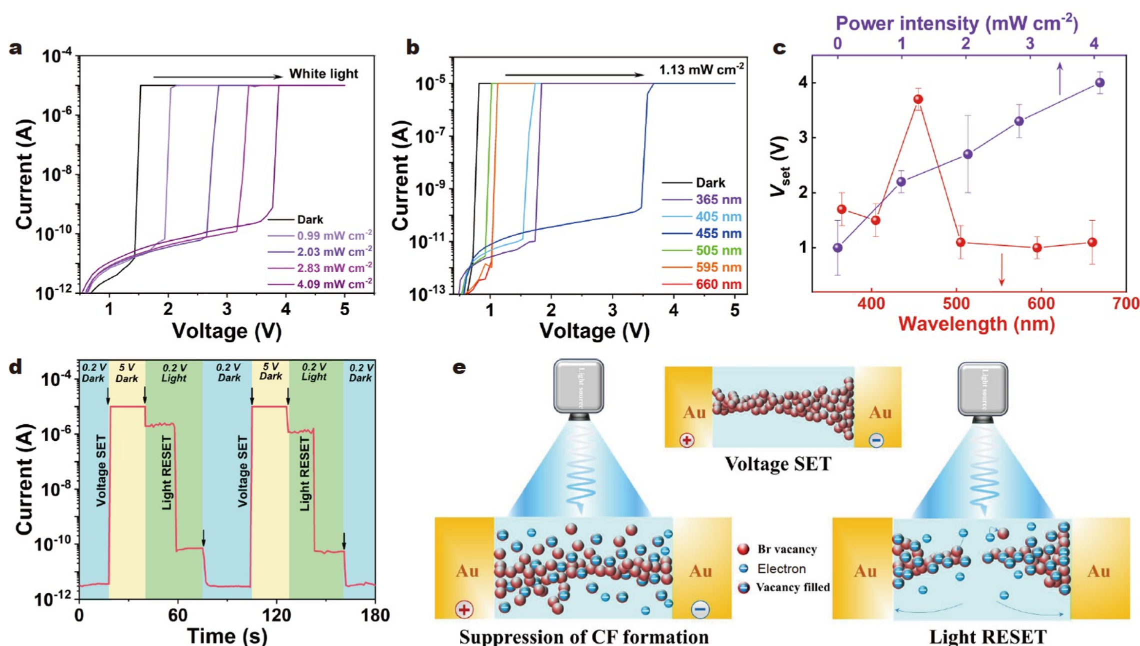

Figure 5 *I-V* characteristics of $Cs_2AgBiBr_6$ (800 nm thick) during the SET process under the light illumination with (a) different intensities and (b) wavelengths. (c) The statistically calculated SET voltage as a function of light intensity and wavelength. (d) Time-dependent current response of the device with separate electrical-writing and optical-erasing processes. The electrical SET and read voltages are 5 and 0.2 V, respectively, and the light of 455 nm with the intensity of 1.13 mW cm^{-2} was used to RESET the device. (e) Schematic diagram of light RESET mechanism.

to LRS, corresponding to an electrical-writing process. Upon illumination at a read voltage of 0.2 V, the current instantly decreased by several orders of magnitude due to the annihilation of CFs. Switching off the light would further reduce the off current and RESET the device to the initial HRS, leading to an optical-erasing process. Thus, periodic voltage SET and light RESET produce an optoelectronic memory with reversible resistance switching up to 10^7. The underlying mechanism of CF annihilation is schematically shown in Fig. 5e. By absorbing photons with an energy higher than the bandgap of $Cs_2AgBiBr_6$, electron-hole pairs can be generated in the channel and subsequently separated by an external electric field. The photo-generated electrons can be captured by the Br vacancies, which seriously suppresses the formation of conductive channels, thereby increasing the V_{set}. Continuous illumination induces more free electrons to fill Br vacancies, resulting in the rupture of CFs in $Cs_2AgBiBr_6$.

CONCLUSIONS

In summary, a high-performance lateral memristor based on the single-crystal double perovskite $Cs_2AgBiBr_6$ has been demonstrated to exhibit an ultralow average SET electric field of 6.67×10^4 V m^{-1} and a high on/off ratio of 10^7. More importantly, the switching behavior of $Cs_2AgBiBr_6$ was found to transition from volatile to nonvolatile resistance switching when its thickness varied from 100 to 800 nm. EDX elemental analysis indicates that the formation of conductive channels in $Cs_2AgBiBr_6$ is attributed to the migration of Br vacancies with low activation energy. Moreover, the formed conductive channels in $Cs_2AgBiBr_6$ can be significantly annihilated by light irradiation with controlled intensity and wavelength, resulting in an optoelectronic memory with separate electrical-writing and optical-erasing steps. Our results provide a comprehensive understanding of ionic migration in single-crystal perovskites and shed light on the future application of perovskite crystals in high-performance and low-power memory devices.

Received 2 April 2022; accepted 11 May 2022;
published online 28 July 2022

1 Burr GW, Shelby RM, Sebastian A, *et al.* Neuromorphic computing using non-volatile memory. Adv Phys-X, 2017, 2: 89–124
2 Kwon DH, Kim KM, Jang JH, *et al.* Atomic structure of conducting nanofilaments in TiO_2 resistive switching memory. Nat Nanotech, 2010, 5: 148–153
3 Yu S, Guan X, Wong HSP. Conduction mechanism of TiN/HfO_x/Pt resistive switching memory: A trap-assisted-tunneling model. Appl Phys Lett, 2011, 99: 063507
4 Lee MJ, Lee CB, Lee D, *et al.* A fast, high-endurance and scalable non-volatile memory device made from asymmetric Ta_2O_{5-x}/TaO_{2-x} bilayer structures. Nat Mater, 2011, 10: 625–630
5 Lee SM, Kim H, Kim DH, *et al.* Tailored 2D/3D halide perovskite heterointerface for substantially enhanced endurance in conducting bridge resistive switching memory. ACS Appl Mater Interfaces, 2020, 12: 17039–17045
6 Choi J, Park S, Lee J, *et al.* Organolead halide perovskites for low operating voltage multilevel resistive switching. Adv Mater, 2016, 28: 6562–6567
7 Gu C, Lee JS. Flexible hybrid organic-inorganic perovskite memory. ACS Nano, 2016, 10: 5413–5418
8 Green MA, Ho-Baillie A, Snaith HJ. The emergence of perovskite solar cells. Nat Photon, 2014, 8: 506–514
9 Heo JH, Han HJ, Kim D, *et al.* Hysteresis-less inverted $CH_3NH_3PbI_3$ planar perovskite hybrid solar cells with 18.1% power conversion efficiency. Energy Environ Sci, 2015, 8: 1602–1608
10 Shin SS, Yeom EJ, Yang WS, *et al.* Colloidally prepared La-doped $BaSnO_3$ electrodes for efficient, photostable perovskite solar cells. Science, 2017, 356: 167–171
11 Dou L, Yang YM, You J, *et al.* Solution-processed hybrid perovskite photodetectors with high detectivity. Nat Commun, 2014, 5: 5404
12 Gu L, Tavakoli MM, Zhang D, *et al.* 3D arrays of 1024-pixel image sensors based on lead halide perovskite nanowires. Adv Mater, 2016,

 © Science China Press and Springer-Verlag GmbH Germany, part of Springer Nature 2022

28: 9713–9721

13 Lian Z, Yan Q, Lv Q, *et al.* High-performance planar-type photodetector on (100) facet of $MAPbI_3$ single crystal. Sci Rep, 2015, 5: 16563

14 Cho H, Jeong SH, Park MH, *et al.* Overcoming the electroluminescence efficiency limitations of perovskite light-emitting diodes. Science, 2015, 350: 1222–1225

15 Zhu H, Fu Y, Meng F, *et al.* Lead halide perovskite nanowire lasers with low lasing thresholds and high quality factors. Nat Mater, 2015, 14: 636–642

16 Zhu X, Lee J, Lu WD. Iodine vacancy redistribution in organic-inorganic halide perovskite films and resistive switching effects. Adv Mater, 2017, 29: 1700527

17 Azpiroz JM, Mosconi E, Bisquert J, *et al.* Defect migration in methylammonium lead iodide and its role in perovskite solar cell operation. Energy Environ Sci, 2015, 8: 2118–2127

18 Game OS, Buchsbaum GJ, Zhou Y, *et al.* Ions matter: Description of the anomalous electronic behavior in methylammonium lead halide perovskite devices. Adv Funct Mater, 2017, 27: 1606584

19 Zhao XG, Yang D, Sun Y, *et al.* Cu-In halide perovskite solar absorbers. J Am Chem Soc, 2017, 139: 6718–6725

20 Zhao XG, Yang JH, Fu Y, *et al.* Design of lead-free inorganic halide perovskites for solar cells *via* cation-transmutation. J Am Chem Soc, 2017, 139: 2630–2638

21 Lei H, Hardy D, Gao F. Lead-free double perovskite $Cs_2AgBiBr_6$: Fundamentals, applications, and perspectives. Adv Funct Mater, 2021, 31: 2105898

22 Igbari F, Wang ZK, Liao LS. Progress of lead-free halide double perovskites. Adv Energy Mater, 2019, 9: 1803150

23 Yin L, Wu H, Pan W, *et al.* Controlled cooling for synthesis of $Cs_2AgBiBr_6$ single crystals and its application for X-ray detection. Adv Opt Mater, 2019, 7: 1900491

24 Zhang Z, Liang Y, Huang H, *et al.* Stable and highly efficient photocatalysis with lead-free double-perovskite of $Cs_2AgBiBr_6$. Angew Chem Int Ed, 2019, 58: 7263–7267

25 Yang J, Bao C, Ning W, *et al.* Stable, high-sensitivity and fast-response photodetectors based on lead-free $Cs_2AgBiBr_6$ double perovskite films. Adv Opt Mater, 2019, 7: 1801732

26 Cheng XF, Qian WH, Wang J, *et al.* Environmentally robust memristor enabled by lead-free double perovskite for high-performance information storage. Small, 2019, 15: 1905731

27 Lao J, Xu W, Jiang C, *et al.* An air-stable artificial synapse based on a lead-free double perovskite $Cs_2AgBiBr_6$ film for neuromorphic computing. J Mater Chem C, 2021, 9: 5706–5712

28 Mao JY, Zheng Z, Xiong ZY, *et al.* Lead-free monocrystalline perovskite resistive switching device for temporal information processing. Nano Energy, 2020, 71: 104616

29 Fang F, Li H, Fang S, *et al.* 2D $Cs_2AgBiBr_6$ with boosted light-matter interaction for high-performance photodetectors. Adv Opt Mater, 2021, 9: 2001930

30 Yang X, Zhou B, Liu C, *et al.* Unravelling a solution-based formation of single-crystalline kinked wurtzite nanowires: The case of MnSe. Nano Res, 2017, 10: 2311–2320

31 Ning W, Zhao XG, Klarbring J, *et al.* Thermochromic lead-free halide double perovskites. Adv Funct Mater, 2019, 29: 1807375

32 Bousoulas P, Panagopoulou M, Boukos N, *et al.* Emulating artificial neuron and synaptic properties with SiO_2-based memristive devices by tuning threshold and bipolar switching effects. J Phys D-Appl Phys, 2021, 54: 225303

33 Wang K, Hu Q, Gao B, *et al.* Threshold switching memristor-based stochastic neurons for probabilistic computing. Mater Horiz, 2021, 8: 619–629

34 Wang J, Lv Z, Xing X, *et al.* Optically modulated threshold switching in core-shell quantum dot based memristive device. Adv Funct Mater, 2020, 30: 1909114

35 Zhang C, Shang J, Xue W, *et al.* Convertible resistive switching characteristics between memory switching and threshold switching in a single ferritin-based memristor. Chem Commun, 2016, 52: 4828–4831

36 Seo JY, Choi J, Kim HS, *et al.* Wafer-scale reliable switching memory based on 2-dimensional layered organic-inorganic halide perovskite. Nanoscale, 2017, 9: 15278–15285

37 Xu Z, Liu Z, Huang Y, *et al.* To probe the performance of perovskite memory devices: Defects property and hysteresis. J Mater Chem C, 2017, 5: 5810–5817

38 Choi J, Le QV, Hong K, *et al.* Enhanced endurance organolead halide perovskite resistive switching memories operable under an extremely low bending radius. ACS Appl Mater Interfaces, 2017, 9: 30764–30771

39 Han JS, Le QV, Choi J, *et al.* Air-stable cesium lead iodide perovskite for ultra-low operating voltage resistive switching. Adv Funct Mater, 2018, 28: 1705783

40 Yang JM, Choi ES, Kim SY, *et al.* Perovskite-related $(CH_3NH_3)_3Sb_2Br_9$ for forming-free memristor and low-energy-consuming neuromorphic computing. Nanoscale, 2019, 11: 6453–6461

41 Cuhadar C, Kim SG, Yang JM, *et al.* All-inorganic bismuth halide perovskite-like materials $A_3Bi_2I_9$ and $A_3Bi_{1.8}Na_{0.2}I_{8.6}$ (A = Rb and Cs) for low-voltage switching resistive memory. ACS Appl Mater Interfaces, 2018, 10: 29741–29749

42 Kim SG, Van Le Q, Han JS, *et al.* Dual-phase all-inorganic cesium halide perovskites for conducting-bridge memory-based artificial synapses. Adv Funct Mater, 2019, 29: 1906686

43 Wang H, Du Y, Li Y, *et al.* Configurable resistive switching between memory and threshold characteristics for protein-based devices. Adv Funct Mater, 2015, 25: 3825–3831

44 Xue W, Liu G, Zhong Z, *et al.* A 1D vanadium dioxide nanochannel constructed *via* electric-field-induced ion transport and its superior metal-insulator transition. Adv Mater, 2017, 29: 1702162

45 Lee JH, Kim GH, Ahn YB, *et al.* Threshold switching in Si-As-Te thin film for the selector device of crossbar resistive memory. Appl Phys Lett, 2012, 100: 123505

46 Song J, Prakash A, Lee D, *et al.* Bidirectional threshold switching in engineered multilayer (Cu_2O/Ag:Cu_2O/Cu_2O) stack for cross-point selector application. Appl Phys Lett, 2015, 107: 113504

47 Lee MJ, Lee D, Cho SH, *et al.* A plasma-treated chalcogenide switch device for stackable scalable 3D nanoscale memory. Nat Commun, 2013, 4: 2629

48 Park J, Hadamek T, Posadas AB, *et al.* Multi-layered $NiO_y/NbO_x/NiO_y$ fast drift-free threshold switch with high I_{on}/I_{off} ratio for selector application. Sci Rep, 2017, 7: 4068

49 Sun Y, Tai M, Song C, *et al.* Competition between metallic and vacancy defect conductive filaments in a $CH_3NH_3PbI_3$-based memory device. J Phys Chem C, 2018, 122: 6431–6436

50 Ghasemi M, Zhang L, Yun JS, *et al.* Dual-ion-diffusion induced degradation in lead-free $Cs_2AgBiBr_6$ double perovskite solar cells. Adv Funct Mater, 2020, 30: 2002342

Acknowledgements Shi Y and Han C acknowledge the financial support from the National Natural Science Foundation of China (61874074 and 62004128), the Fundamental Research Foundation of Shenzhen (JCYJ20190808152607389), and the (Key) Project of Department of Education of Guangdong Province (2016KZDXM008). Li H acknowledges the support from Guangdong Basic and Applied Basic Research Foundation (General Program, 2022A1515012055), the Natural Science Foundation of Shenzhen University (2017011) and the Technology and Innovation Commission of Shenzhen (20200810164814001). This project was also funded by Shenzhen Peacock Plan (KQTD2016053112042971). The authors thank the technical support from the Instrumental Analysis Center and the Photonics Center of Shenzhen University.

Author contributions You Q designed and engineered the experiments; Huang F and Fang F performed the material synthesis; Zhu J, Zheng Y, Fang S, Zhou B, and Li H participated in the characterizations and revised the manuscript; You Q wrote the paper with support from Han C and Shi Y. All authors contributed to the general discussion.

Conflict of interest The authors declare that they have no conflict of interest.

© Science China Press and Springer-Verlag GmbH Germany, part of Springer Nature 2022

Supplementary information Supporting data are available in the online version of the paper.

Qi You is currently a doctoral candidate at the Institute of Microscale Optoelectronics, Shenzhen University (SZU, China). His research interests mainly focus on the electronic memory devices based on transition metal dichalcogenides and metal halide perovskites.

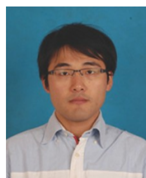

Cheng Han is currently a tenured associated professor at the Institute of Microscale Optoelectronics of SZU. He received his PhD degree in physics from the National University of Singapore (NUS, Singapore) in 2014. His research interests include the fabrication and interface engineering of low-dimensional materials-based electronic and optoelectronic devices.

Yumeng Shi is currently a full professor at the College of Electronics and Information Engineering, SZU. He received his PhD degree in materials science and engineering from Nanyang Technological University (NTU, Singapore) in 2011. He is a "Global Highly Cited Researcher" by Clarivate Analytics and Elsevier. His current research interests include the synthesis of low-dimensional materials and their applications in optoelectronics.

具有超低开关电场的可控的易失性至非易失性单晶无铅双钙钛矿忆阻器

游琪[1], 黄富[1], 房菲儿[2], 祝家齐[1], 郑越[1], 方绍帆[2], 周勃[2], 李贺楠[2], 韩成[1*], 时玉萌[2*]

摘要 全无机无铅双钙钛矿由于其优异的电子传输能力、高光敏性、低毒性和环境稳定性，为电子/光电存储器件提供了潜在的材料. 然而，钙钛矿薄膜的多晶性质严重限制了器件性能. 在此，我们展示了一种基于单晶双钙钛矿$Cs_2AgBiBr_6$的高性能忆阻器，其具有6.67×10^4 V m^{-1}的超低开关电场和10^7的高电流开/关比. 值得注意的是，$Cs_2AgBiBr_6$的电阻开关行为与单晶钙钛矿的厚度相关，当单晶厚度从100到800 nm变化时，忆阻器从易失性的阈值开关行为演变为非易失性的忆阻开关行为. 元素分析表明，$Cs_2AgBiBr_6$中导电通道的形成与具有低活化能Br空位的迁移有关. 此外，形成的导电通道可以被具有不同波长和强度的光照湮灭，从而实现具有单独的电写入和光擦除的光电存储器. 我们的研究结果为单晶钙钛矿中的离子迁移提供了深刻的见解，并为其在未来的电子和光电存储器中的应用提供了理论基础.

© Science China Press and Springer-Verlag GmbH Germany, part of Springer Nature 2022